

Wavelength-division multiplexing optical Ising simulator enabling fully programmable spin couplings and external magnetic fields

Li Luo, Zhiyi Mi, Junyi Huang, and Zhichao Ruan*

*Interdisciplinary Center of Quantum Information,
State Key Laboratory of Modern Optical Instrumentation,
and Zhejiang Province Key Laboratory of Quantum Technology and Device,
Department of Physics, Zhejiang University, Hangzhou 310027, China*

Recently, spatial photonic Ising machines (SPIMs) have demonstrated the abilities to compute the Ising Hamiltonian of large-scale spin systems, with the advantages of ultrafast speed and high power efficiency. However, such optical computations have been limited to specific Ising models with fully connected couplings. Here we develop a wavelength-division multiplexing SPIM to enable programmable spin couplings and external magnetic fields as well for general Ising models. We experimentally demonstrate such a wavelength-division multiplexing SPIM with a single spatial light modulator, where the gauge transformation is implemented to eliminate the impact of pixel alignment. To show the programmable capability of general spin coupling interactions, we explore three spin systems: $\pm J$ models, Sherrington-Kirkpatrick models, and only locally connected J_1 - J_2 models and observe the phase transitions between the spin-glass, ferromagnetic and paramagnetic phases. These results show that the wavelength-division multiplexing approach has great programmable flexibility of spin couplings and external magnetic fields, which provides the opportunities to solve general combinatorial optimization problems with large-scale and on-demand SPIM.

Ising model is an archetypal model widely used for investigations of complex dynamics in physics, computer science, biology, and even social systems. Owing to Moore's law for conventional computers, there has been tremendous interest and a boost in the development of unconventional computing architectures for simulating Ising Hamiltonians, for example, based on optical parametric oscillators [1–5], lasers [6–10], polariton [11–13], trapped ions [14], atomic and photonic condensates [15, 16], electronic memorisers [17], superconducting qubits [18–20], and nanophotonics circuits [21–25]. Despite different approaches and technologies, it is worth noting that the error probability and time-to-solution metrics of these Ising machines have similar scaling trend as a function of the number of spins [26]. Practically, the difficulty to implement the spin coupling interactions with the proposed hardware has become the main factor limiting scalability and performance for unconventional Ising simulators [27, 28].

In this regard, by encoding spins on the phase terms of a monochromatic field with spatial light modulators (SLMs), spatial photonic Ising machines (SPIMs) benefit with reliable large-scale Ising spin systems, even up to thousands of spins by exploring the spatial degrees of freedom [29–39]. Like other optical analog computations [40–50], the calculation of spin system energy is just by instantaneously measuring the light intensity, therefore with ultrafast speed and high power efficiency [33]. Moreover, to eliminate the impact of pixel alignment, the gauge transformation is proposed to simultaneously encode spin configurations and interaction strengths with a single spatial phase modulator [35]. However, the original proposed SPIM [33] is only applicable to Mattis-type

coupling interactions [51]. Even with scattering medium, tunable SPIM was demonstrated based on multiple light scattering, while the Ising spin system is still limited to specific fully connected couplings [38]. Therefore, how to realize completely programmable spin couplings is a primary target to develop SPIMs for general Ising models.

Here we report a wavelength-division multiplexing SPIM to enable fully programmable spin couplings and external magnetic fields as well. Beyond Mattis-type interaction, we propose a gauge transformation for general Ising models with arbitrary spin interactions. More importantly, with wavelength-division multiplexing, we optically compute the general spin Hamiltonian with the advantages of large scale and ultrafast speed. We experimentally demonstrate such a wavelength-division multiplexing SPIM with a single SLM, where the gauge transformation is implemented to eliminate the impact of pixel alignment. To show the programmable capability of general spin coupling interactions, we explore three kinds of Ising models: fully connected $\pm J$ model, Sherrington-Kirkpatrick (SK) model, and only locally connected J_1 - J_2 model. For $\pm J$ and SK models, we investigate the process of phase transition with different spin interactions and experimentally observe the spin-glass (SG), ferromagnetic (FM), and paramagnetic (PM) phases by simulating the equilibrium systems at different temperatures. We verify that the critical temperatures evaluated by the wavelength-division multiplexing SPIM are consistent with the predictions of the mean-field theory. We also demonstrate the phase transition from PM to stripe-antiferromagnetic phase in the J_1 - J_2 model with competing interactions and experimentally observe the presence of SG phase by increasing the stochasticity of the next-nearest-neighbor interactions. These results show the great programmable flexibility of spin couplings and external magnetic fields by the wavelength-division

* zhichao@zju.edu.cn

multiplexing SPIM, which provides important potential applications in solving combinatorial optimization problems.

The wavelength-division multiplexing SPIM, designed for full programmability of spin interactions and magnetic fields, is shown in Fig. 1(a). The illumination components consist of a collimated super-continuum laser, a diffraction grating, and a cylindrical lens. The diffraction grating and cylindrical lens diffract light with different wavelengths onto a SLM along the x -axis, while the y -axis pixels are illuminated coherently by the same wavelength. By adjusting the diffraction angle, the operation wavelengths are selected within the quasi-stationary region of supercontinuum light [52]. The optical field modulated by the SLM is then transformed by a Fourier lens, resulting in an incoherent intensity summation of different wavelengths and coherent interference for each wavelength at the back focus plane.

Next we show that the wavelength-division multiplexing SPIM can optically compute the Hamiltonian of any Ising model by detecting the intensity at the center position of the back focus plane. The Ising model is given by $H = -\sum_{i \neq j} J_{ij} \sigma_i \sigma_j - \sum_i h_i \sigma_i$, where J_{ij} and h_i are the interaction strength and the external magnetic field strength for N spins, respectively, and σ_i can take binary values $+1$ or -1 . By adding an auxiliary spin with $\sigma_{N+1} = 1$, we use a Cholesky-like decomposition to transform the Hamiltonian into multiple Mattis models $H_k = -\sum_{i,j=k}^{N+1} J \kappa_i^k \kappa_j^k \sigma_i \sigma_j$, so that $H = \sum_{k=1}^N H_k + H_0$. The interaction strength for the k -th Mattis model is given by $J_{ij}^k = J \kappa_i^k \kappa_j^k$, where $|\kappa_i^k| \leq 1$, J and H_0 are constants with the unit of energy. The transformation is summarized in Sec. I of the Supplemental Material (SM), and we note that despite the transformation, the degrees of freedom of κ_i^k remain equal to $N(N+1)/2$, which is the summation of those of $\{J_{ij}\}$ and $\{h_i\}$ for arbitrary interactions and magnetic fields.

Inspired by the encoding scheme for Mattis model [35, 36], here we propose a general one for arbitrary Ising models by a gauge transformation. This transformation allows to encode the spin configurations and program the interaction strengths on a single phase-only SLM, as shown in Fig. 1(b). The transformation rotates each original spin about the z -axis by an angle $\alpha_j^k = \arccos \kappa_j^k$ to arrive at a new spin vector, which is then projected onto the z -axis to obtain the effective spin $\sigma_j'^k = \kappa_j^k \sigma_j$. By the gauge transformation given as

$$\sigma_j \rightarrow \sigma_j'^k, \quad J_{ij}^k \rightarrow J, \quad (1)$$

the transformed Hamiltonian remains invariant, $H = -J \sum_{k=1}^N \sum_{i,j=k}^{N+1} \sigma_i'^k \sigma_j'^k + H_0$, where the interactions of the transformed spins are uniform with a strength of J in both short and long ranges.

We encode the gauge-transformed spin configurations $\sigma_j'^k$ on a single phase-only SLM with wavelength-division multiplexing. For the k -th Mattis model, we assume a

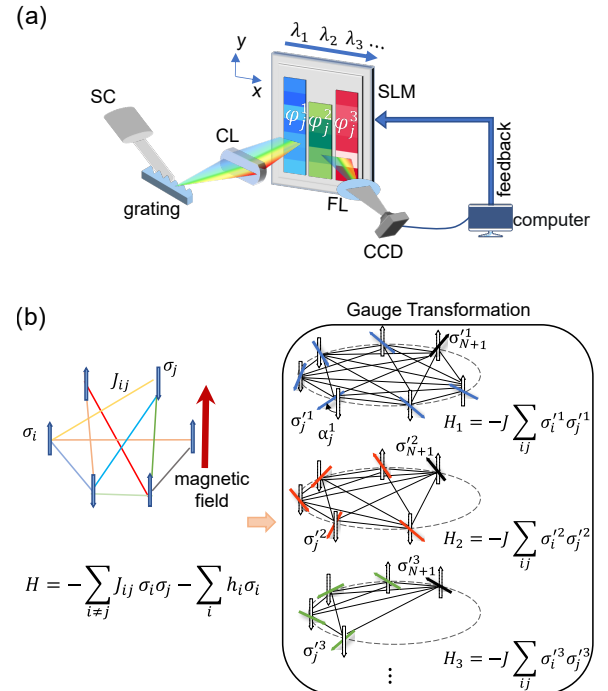


FIG. 1. (a) Schematic of the wavelength-division multiplexing SPIM. In this setup, light with different wavelengths is diffracted and focus on a phase-only spatial light modulator (SLM) along the x -direction, while the pixels in the y -direction are coherently illuminated by incident light of the same wavelength. The spins are encoded with phase modulation on the SLM using Eq. (2). SC: super-continuum laser; CL: cylindrical lens; FL: Fourier lens; CCD: charge coupled device camera. (b) The Ising model with general interactions and external magnetic fields is transformed into N numbers of Mattis models via gauge transformation, and $H = \sum_{k=1}^N H_k + H_0$, where $H_k = -J \sum_{i,j=k}^{N+1} \sigma_i'^k \sigma_j'^k$ and J and H_0 are constants. Here $\sigma_j'^k$ represents the z component of spin σ_j rotated by an angle α_j^k with respect to the z axis.

uniform spectrum intensity illuminating on SLM and apply a phase modulation on the y -directional pixels for each spin as

$$\varphi_j^k = \sigma_j \frac{\pi}{2} + (-1)^j \alpha_j^k. \quad (2)$$

We note that for each Mattis model, the phase modulation should account for the calibration of different wavelengths when encoding φ_j^k in the x direction on the SLM. The normalized intensity \tilde{I} at the center position of the back focus plane is the summation of the incoherent field intensities for light with different wavelengths, $\tilde{I} = \sum_{k=1}^N \sum_{i,j=k}^{N+1} \sigma_i'^k \sigma_j'^k$. The Ising Hamiltonian for the general spin interactions is thus optically computed as $H = -J\tilde{I} + H_0$. The details of the gauge transformation and the encoding for general illumination cases are described in SM Sec. II.

To evaluate the performance of the wavelength-division multiplexing SPIM, we conduct an experiment (detailed

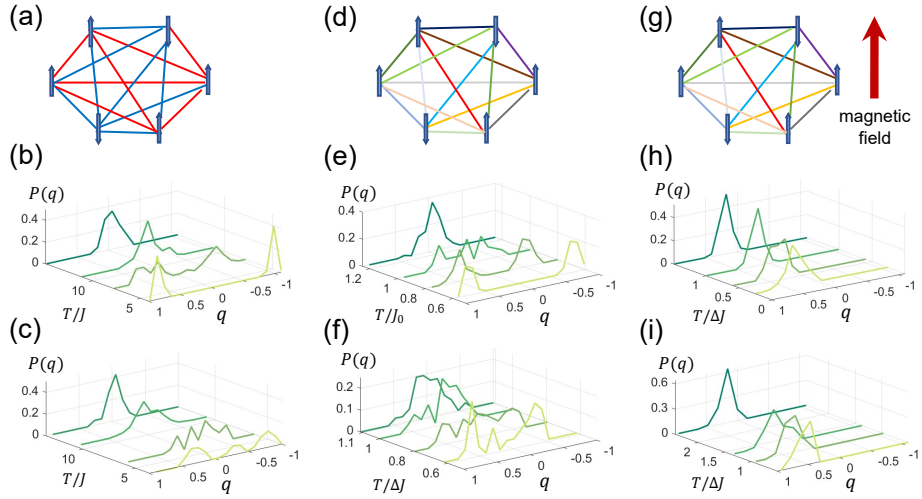


FIG. 2. Probability distribution of the Parisi parameter q as a function of T , for $N = 80$ spins. (a) Schematic representation for the $\pm J$ model. (b) and (c) present the experimental results for $p = 0.7$ and 0.55 , respectively. (d) Schematic for the SK model. (e) and (f) display the results for $J_0 = 40$ and 8 , respectively, with $\Delta J = \sqrt{80}$ fixed. (g) Schematic for the SK model with a uniform external magnetic field. (h) and (i) present the results for $h = 0.2$ and 2 , respectively, with J_0 and ΔJ being the same as (f).

experiment setup can be found in SM Sec.III) and simulate three well-studied spin systems: the $\pm J$ model [Fig. 2(a)], the SK model [Fig. 2(d)] and the SK model under external magnetic field [Fig. 2(g)]. The interactions between spins in the $\pm J$ model are either 1 with a probability of p or -1 with a probability of $1 - p$. The probability distribution is given as $P(J_{ij}) = p\delta(J_{ij} - J) + (1 - p)\delta(J_{ij} + J)$, where $\delta(x)$ is a Kronecker delta function equal to 1 for $x = 0$ and 0 for other cases. In the SK model, the probability distribution of J_{ij} is Gaussian, with the distribution given as $P(J_{ij}) = \mathcal{N}(J_{ij}; \frac{J_0}{N}, \frac{\Delta J^2}{N})$, where J_0 and ΔJ are two constant parameters, such that the energy can be extensive and proportional to N [53].

We use the wavelength-division multiplexing SPIM to examine the phase transition with 80 spins. For each model, a quenched realization is generated for the interactions J_{ij} randomly assigned based on their respective probability distributions. By varying the temperature and utilizing the Markov chain Monte Carlo algorithm, we generate 100 replicas from the final configuration, where each replica is obtained by randomly initializing spin configurations and through 800 iterations of the optical Metropolis Hasting sampling procedure [34, 35, 54]. The spin overlap is then calculated as $q_{\alpha\beta} = \frac{1}{N} \sum_{i=1}^N \sigma_i^\alpha \sigma_i^\beta$, which measures the similarity between replicas α and β . The phase transition is characterized by the probability density function $P(q)$ of the overlap.

Figures 2(b) and (c) present the experimental results for the $\pm J$ model with the parameters $p = 0.7$ and 0.55 , respectively. At high temperatures, both of the two parameters $p = 0.7$ and $p = 0.55$ result in randomly ar-

ranged spins and little correlation between replicas, indicating the PM phase, where $P(q)$ has a peak at around zero. At low temperatures, however, $P(q)$ displays the distinct density distributions for the two values of p . For $p = 0.7$, since the interactions are mostly positive, the spins attract each other and the replicas remain in only two ground states of the FM phase. Consequently, $P(q)$ at low temperature has two peaks around 1 and -1 as shown in Fig. 2(b). On the other hand, for $p = 0.55$, the interactions are composed of both positive and negative values, causing frustration during the energy minimization process at low temperatures. This frustration results in a multi-valley energy landscape and $P(q)$ takes on a wide range of values at low temperature, as depicted in Fig. 2(c). This feature of widely distributed q is the hallmark of the SG phase. These results demonstrate that the SG phase transition indeed emerges in the systems simulated by the wavelength-division multiplexing SPIM.

To further study the phase transition with the wavelength-division multiplexing SPIM, we examine the SK model without magnetic fields and compare the estimated critical temperature with the mean-field theory. Fig. 2(e) and (f) show the results for $J_0 = 40$ and 8 , respectively, with $\Delta J = \sqrt{80}$. At high temperatures, both figures show the PM phase with $P(q)$ dominated around zero, due to the randomly arranged spin configurations. However, as shown in Figs. 2(e) and (f), $P(q)$ at low temperatures exhibit the FM and SG phases for the different values of J_0 and occur around $T_c = J_0$ and $T_c = \Delta J$, respectively. The experiment results are consistent with the mean-field theory [53] with the critical temperatures for the PM-FM transition and for the PM-SG transition.

Additionally, we also investigate the stability of the complex multi-valley energy landscape of the SG phase

in the presence of a uniform external magnetic field in the SK model [Fig. 2(g)]. As shown in Fig. 2(h), for the SK model with $J_0 = 8$ and $\Delta J = \sqrt{80}$, a weak magnetic field with $h = 0.2$ aligns spins with the field direction even at high temperature, causing most q values to cluster around positive values. Upon decreasing the temperature, the probability distribution of q resembles that of the SG phase covering a wide range, indicating that weak magnetic fields are not strong enough to completely alter the multi-valley energy landscape. However, when subjected to a stronger magnetic field with $h = 2$ [Fig. 2(i)], at low temperatures q are more clustered, which suggests that the magnetic field flattens out some valleys in the energy landscape.

The wavelength-division multiplexing SPIM can be utilized to study Ising systems beyond the full-coupling models. To demonstrate its full programmability of spin couplings, we examine a locally connected J_1 - J_2 model [Fig. 3(a)]. The Hamiltonian only includes nearest-neighbor ferromagnetic and next-nearest-neighbor antiferromagnetic interactions on a square lattice with cyclic boundary conditions: $H = -J_1 \sum_{\langle ij \rangle} \sigma_i \sigma_j - J_2 \sum_{\langle\langle ij \rangle\rangle} \sigma_i \sigma_j$,

where $\langle \rangle$ and $\langle\langle \rangle\rangle$ denote the nearest and next-nearest neighbors, respectively. The nearest-neighbor ferromagnetic interactions align adjacent spins with $J_1 > 0$ (represented by solid lines in Fig. 3(a)), while the next-nearest-neighbor antiferromagnetic interactions drive two adjacent rows and columns to have opposite orientations with $J_2 < 0$ (represented by double parallel lines). When the antiferromagnetic interaction J_2 is strong enough to overcome the ferromagnetic interaction J_1 , a striped phase is produced, characterized by a two-component order parameter (m_x, m_y) , where $m_x = \frac{1}{N} \sum_{i=1}^N \sigma_i (-1)^{x_i}$, and $m_y = \frac{1}{N} \sum_{i=1}^N \sigma_i (-1)^{y_i}$, and (x_i, y_i) are the coordinates of spin σ_i . The ground states of the J_1 - J_2 model are \mathbb{Z}_4 ordered when $|J_2|/J_1 > 1/2$, and can be represented by the order parameters of $(m_x, m_y) = (\pm 1, 0)$ and $(m_x, m_y) = (0, \pm 1)$, corresponding to two longitudinal and transverse striped states with opposite spin directions [55].

Using the wavelength-division multiplexing SPIM, we simulate the transition between the striped states and the PM phases. Fig. 3(b) shows the simulation results for the parameters $J_1 = 0.2$ and $J_2 = -1$ on an 8×8 lattice. Above the critical temperature of $T_c = 20J_1$, the order parameters (m_x, m_y) are both close to zero due to the thermal fluctuations destroying the long-range correlation between spins as a sample of spin configurations shown in Fig. 3(c). However, below T_c , the order parameters split into four clusters located in different quadrants, corresponding to the four striped states [Fig. 3(b)]. Figs. 3(d-g) show four samples of the spin configurations, which exhibit a long stripe spatial distribution. These results for the J_1 - J_2 model demonstrate the programmability of spin couplings.

The J_1 - J_2 model plays a crucial role in comprehending the low-temperature phase of short-range spin glass.

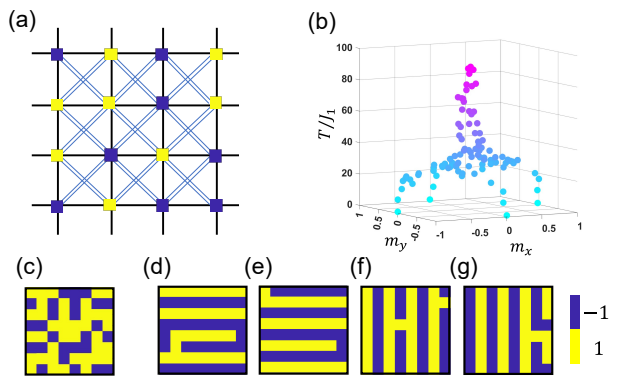


FIG. 3. Experimental results for a locally connected J_1 - J_2 model with cyclic boundary condition. (a) A schematic of the J_1 - J_2 model, where the thick solid line indicates the nearest neighbor ferromagnetic interaction ($J_1 > 0$) and the blue double line represents the next-nearest-neighbor antiferromagnetic interaction ($J_2 < 0$). Blue and yellow squares denote spins $\sigma_i = -1$ and 1, respectively, and the experiment was conducted on an 8×8 lattice. (b) Results for the order parameter (m_x, m_y) as a function of T , for the parameters $J_1 = 0.2$ and $J_2 = -1$. (c) A spin configuration sampled at $T = 70J_1$ representing a PM state. (d-g) Four spin configurations sampled at $T = 14.39J_1$ which are adjacent to four striped states, respectively.

With the help of the wavelength-division multiplexing SPIM, we consider the next-nearest-neighbor interactions are Gaussian as $P(J_2) = \mathcal{N}(J_2; J_0, \Delta J^2)$ with a mean value of $J_0 = -1$ and a standard deviation ΔJ , while maintaining a fixed value of nearest-neighbor interactions $J_1 = 1$. For small variances of $\Delta J = 0.2$ [Fig. 4(a)], the density distribution of q exhibits a single peak at high temperatures, signifying the PM phase. However, as the temperature decreases, $P(q)$ transforms into three clusters of peaks, indicative of the \mathbb{Z}_4 ordered striped ground states. The peak around $q = 0$ is twice as high as those around $q = \pm 1$. In contrast, by increasing the standard deviation to $\Delta J = 2$, the increased disorder in the next-nearest-neighbor interactions results in a SG phase at low temperatures. The SG phase is characterized by many pairs of ground states and results in multiple sharp peaks of $P(q)$ as Fig. 4(b).

We also experimentally measure the susceptibility $\chi = \frac{1}{N} \sum_{i=1}^N \frac{1-m_i^2}{T}$ [56] to investigate the transition temperature in the J_1 - J_2 model, where m_i represents the time ensemble average of σ_i . At high temperatures, thermodynamic fluctuations cause the spin orientation to constantly change, resulting in m_i being close to zero, as shown in Fig. 4(c). The susceptibility in both two cases decreases with increasing temperature and scales with $\frac{1}{T}$. The results also indicate that the critical temperatures are different, with $T_c = 14J_1$ and $T_c = 10J_1$ for $\Delta J = 0.2$ and $\Delta J = 2$, respectively. In the case of $\Delta J = 0.2$, the interactions of the next-nearest-neighbors are relatively small and close to -1 . As the temperature decreases below T_c , the system reaches the striped

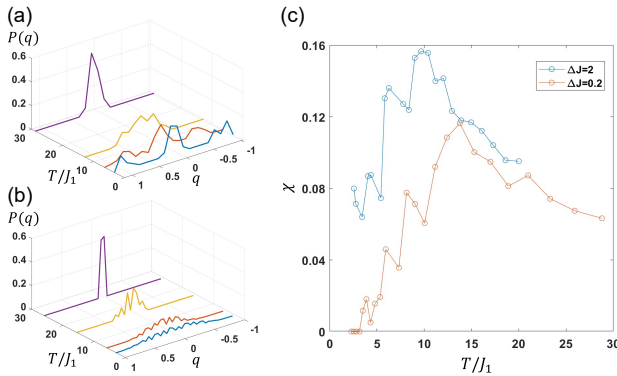


FIG. 4. (a) and (b) Probability density distribution of q for the J_1 - J_2 models with the fixed nearest neighbor interactions $J_1 = 1$, while the next-nearest-neighbor interactions are Gaussian distributed with the mean value of $J_0 = -1$ and the standard deviation of $\Delta J = 0.2$ and 2, respectively. (c) Experimental measured susceptibility for $\Delta J = 0.2$ and $\Delta J = 2$.

ground states with m_i approaching ± 1 , causing the average susceptibility χ to converge to zero. In contrast, for $\Delta J = 2$, at low temperatures, the local spin orienta-

tion still varies slowly due to the presence of numerous ground states in the SG phase, resulting in χ being close to a non-zero constant. These experimental results clearly demonstrate the spin-glass phase transition in the J_1 - J_2 model with short-range interactions.

In summary, we propose the wavelength-division multiplexing SPIM to realize fully programmable spin couplings and external magnetic fields. With the full-coupling $\pm J$ models, SK models and the only locally connected J_1 - J_2 models, we demonstrate the great programmable flexibility of spin couplings and external magnetic fields with the wavelength-division multiplexing SPIM. By simulating the equilibrium systems at different temperatures, we experimentally observe the phase transitions between the spin-glass, ferromagnetic and paramagnetic phases with the wavelength-division multiplexing SPIM. The exhibited rich phase diagrams are beneficial to searching for the true ground state of the Ising model, and thus the wavelength-division multiplexing approach provides important potential applications in solving combinatorial optimization problems.

The authors acknowledge funding through the National Key Research and Development Program of China (2022YFA1405200) and the National Natural Science Foundation of China (12174340).

[1] P. L. McMahon, A. Marandi, Y. Haribara, R. Hamerly, C. Langrock, S. Tamate, T. Inagaki, H. Takesue, S. Utsunomiya, K. Aihara, *et al.*, A fully programmable 100-spin coherent Ising machine with all-to-all connections, *Science* **354**, 614 (2016).

[2] T. Inagaki, Y. Haribara, K. Igarashi, T. Sonobe, S. Tamate, T. Honjo, A. Marandi, P. L. McMahon, T. Umeki, K. Enbutsu, *et al.*, A coherent Ising machine for 2000-node optimization problems, *Science* **354**, 603 (2016).

[3] T. Inagaki, K. Inaba, R. Hamerly, K. Inoue, Y. Yamamoto, and H. Takesue, Large-scale Ising spin network based on degenerate optical parametric oscillators, *Nature Photonics* **10**, 415 (2016).

[4] F. Böhm, G. Verschaffelt, and G. Van der Sande, A poor man's coherent Ising machine based on opto-electronic feedback systems for solving optimization problems, *Nature Communications* **10**, 1 (2019).

[5] A. Marandi, Z. Wang, K. Takata, R. L. Byer, and Y. Yamamoto, Network of time-multiplexed optical parametric oscillators as a coherent Ising machine, *Nature Photonics* **8**, 937 (2014).

[6] S. Utsunomiya, K. Takata, and Y. Yamamoto, Mapping of Ising models onto injection-locked laser systems, *Optics Express* **19**, 18091 (2011).

[7] M. Babaeian, D. T. Nguyen, V. Demir, M. Akbulut, P.-A. Blanche, Y. Kaneda, S. Guha, M. A. Neifeld, and N. Peyghambarian, A single shot coherent Ising machine based on a network of injection-locked multicore fiber lasers, *Nature Communications* **10**, 1 (2019).

[8] C. Tradonsky, I. Gershenzon, V. Pal, R. Chriki, A. A. Friesem, O. Raz, and N. Davidson, Rapid laser solver for the phase retrieval problem, *Science Advances* **5**, eaax4530 (2019).

[9] M. Parto, W. Hayenga, A. Marandi, D. N. Christodoulides, and M. Khajavikhan, Realizing spin Hamiltonians in nanoscale active photonic lattices, *Nature Materials* **19**, 725 (2020).

[10] M. Honari-Latifpour and M.-A. Miri, Mapping the XY Hamiltonian onto a network of coupled lasers, *Physical Review Research* **2**, 043335 (2020).

[11] K. P. Kalinin, A. Amo, J. Bloch, and N. G. Berloff, Polaritonic XY-Ising machine, *Nanophotonics* **9**, 4127 (2020).

[12] N. G. Berloff, M. Silva, K. Kalinin, A. Askitopoulos, J. D. Töpfer, P. Cilibrizzi, W. Langbein, and P. G. Lagoudakis, Realizing the classical XY Hamiltonian in polariton simulators, *Nature Materials* **16**, 1120 (2017).

[13] K. P. Kalinin and N. G. Berloff, Simulating Ising and n-state planar potts models and external fields with nonequilibrium condensates, *Physical Review Letters* **121**, 235302 (2018).

[14] K. Kim, M.-S. Chang, S. Korenblit, R. Islam, E. E. Edwards, J. K. Freericks, G.-D. Lin, L.-M. Duan, and C. Monroe, Quantum simulation of frustrated Ising spins with trapped ions, *Nature* **465**, 590 (2010).

[15] J. Struck, M. Weinberg, C. Ölschläger, P. Windpassinger, J. Simonet, K. Sengstock, R. Höppner, P. Hauke, A. Eckardt, M. Lewenstein, *et al.*, Engineering Ising-XY spin-models in a triangular lattice using tunable artificial gauge fields, *Nature Physics* **9**, 738 (2013).

[16] B. Kassenberg, M. Vretenar, S. Bissesar, and J. Klaers, Controllable Josephson junction for photon Bose-Einstein condensates, *arXiv preprint arXiv:2001.09828* (2020).

[17] F. Cai, S. Kumar, T. Van Vaerenbergh, X. Sheng, R. Liu, C. Li, Z. Liu, M. Foltin, S. Yu, Q. Xia, J. J. Yang, R. Beausoleil, W. D. Lu, and J. P. Strachan, Power-efficient combinatorial optimization using intrinsic noise in memristor hopfield neural networks, *Nature Electronics* **3**, 409 (2020).

[18] M. W. Johnson, M. H. S. Amin, S. Gildert, T. Lanting, F. Hamze, N. Dickson, R. Harris, A. J. Berkley, J. Johansson, P. Bunyk, *et al.*, Quantum annealing with manufactured spins, *Nature* **473**, 194 (2011).

[19] S. Boixo, T. F. Rønnow, S. V. Isakov, Z. Wang, D. Wecker, D. A. Lidar, J. M. Martinis, and M. Troyer, Evidence for quantum annealing with more than one hundred qubits, *Nature Physics* **10**, 218 (2014).

[20] A. D. King, J. Carrasquilla, J. Raymond, I. Ozfidan, E. Andriyash, A. Berkley, M. Reis, T. Lanting, R. Harris, F. Altomare, *et al.*, Observation of topological phenomena in a programmable lattice of 1,800 qubits, *Nature* **560**, 456 (2018).

[21] C. Roques-Carmes, Y. Shen, C. Zanoci, M. Prabhu, F. Atieh, L. Jing, T. Dubček, C. Mao, M. R. Johnson, V. Čeperić, *et al.*, Heuristic recurrent algorithms for photonic Ising machines, *Nature Communications* **11** (2020).

[22] M. Prabhu, C. Roques-Carmes, Y. Shen, N. Harris, L. Jing, J. Carolan, R. Hamerly, T. Baehr-Jones, M. Hochberg, V. Čeperić, *et al.*, Accelerating recurrent Ising machines in photonic integrated circuits, *Optica* **7**, 551 (2020).

[23] Y. Shen, N. C. Harris, S. Skirlo, M. Prabhu, T. Baehr-Jones, M. Hochberg, X. Sun, S. Zhao, H. Larochelle, D. Englund, *et al.*, Deep learning with coherent nanophotonic circuits, *Nature Photonics* **11**, 441 (2017).

[24] K. Wu, J. G. De Abajo, C. Soci, P. P. Shum, and N. I. Zheludev, An optical fiber network oracle for NP-complete problems, *Light: Science & Applications* **3**, e147 (2014).

[25] Y. Okawachi, M. Yu, J. K. Jang, X. Ji, Y. Zhao, B. Y. Kim, M. Lipson, and A. L. Gaeta, Demonstration of chip-based coupled degenerate optical parametric oscillators for realizing a nanophotonic spin-glass, *Nature Communications* **11**, 1 (2020).

[26] N. Mohseni, P. L. McMahon, and T. Byrnes, Ising machines as hardware solvers of combinatorial optimization problems, *Nature Reviews Physics* **4**, 363 (2022).

[27] B. Heim, T. F. Rønnow, S. V. Isakov, and M. Troyer, Quantum versus classical annealing of ising spin glasses, *Science* **348**, 215 (2015).

[28] R. Hamerly, T. Inagaki, P. L. McMahon, D. Venturelli, A. Marandi, T. Onodera, E. Ng, C. Langrock, K. Inaba, T. Honjo, *et al.*, Experimental investigation of performance differences between coherent Ising machines and a quantum annealer, *Science Advances* **5**, eaau0823 (2019).

[29] S. Kumar, H. Zhang, and Y.-P. Huang, Large-scale Ising emulation with four body interaction and all-to-all connections, *Communications Physics* **3**, 1 (2020).

[30] D. Pierangeli, M. Rafayelyan, C. Conti, and S. Gigan, Scalable spin-glass optical simulator, *Physical Review Applied* **15**, 034087 (2021).

[31] D. Pierangeli, G. Marcucci, and C. Conti, Adiabatic evolution on a spatial-photonic Ising machine, *Optica* **7**, 1535 (2020).

[32] D. Pierangeli, G. Marcucci, D. Brunner, and C. Conti, Noise-enhanced spatial-photonic Ising machine, *Nanophotonics* **9**, 4109 (2020).

[33] D. Pierangeli, G. Marcucci, and C. Conti, Large-scale photonic Ising machine by spatial light modulation, *Physical Review Letters* **122**, 213902 (2019).

[34] M. Leonetti, E. Hörmann, L. Leuzzi, G. Parisi, and G. Ruocco, Optical computation of a spin glass dynamics with tunable complexity, *Proceedings of the National Academy of Sciences* **118**, e2015207118 (2021).

[35] Y. Fang, J. Huang, and Z. Ruan, Experimental observation of phase transitions in spatial photonic ising machine, *Physical Review Letters* **127**, 043902 (2021).

[36] J. Huang, Y. Fang, and Z. Ruan, Antiferromagnetic spatial photonic ising machine through optoelectronic correlation computing, *Communications Physics* **4**, 1 (2021).

[37] W. Sun, W. Zhang, Y. Liu, Q. Liu, and Z. He, Quadrature photonic spatial ising machine, *Optics Letters* **47**, 1498 (2022).

[38] G. Jacucci, L. Delloye, D. Pierangeli, M. Rafayelyan, C. Conti, and S. Gigan, Tunable spin-glass optical simulator based on multiple light scattering, *Physical Review A* **105**, 033502 (2022).

[39] S. Kumar, Z. Li, T. Bu, C. Qu, and Y. Huang, Observation of distinct phase transitions in a nonlinear optical ising machine, *Communications Physics* **6**, 31 (2023).

[40] A. Silva, F. Monticone, G. Castaldi, V. Galdi, A. Alù, and N. Engheta, Performing mathematical operations with metamaterials, *Science* **343**, 160 (2014).

[41] D. A. Bykov, L. L. Doskolovich, E. A. Bezus, and V. A. Soifer, Optical computation of the laplace operator using phase-shifted bragg grating, *Optics Express* **22**, 25084 (2014).

[42] Z. Ruan, Spatial mode control of surface plasmon polariton excitation with gain medium: from spatial differentiator to integrator, *Optics Letters* **40**, 601 (2015).

[43] A. Youssefi, F. Zangeneh-Nejad, S. Abdollahramezani, and A. Khavasi, Analog computing by brewster effect, *Optics Letters* **41**, 3467 (2016).

[44] T. Zhu, Y. Zhou, Y. Lou, H. Ye, M. Qiu, Z. Ruan, and S. Fan, Plasmonic computing of spatial differentiation, *Nature Communications* **8**, 1 (2017).

[45] W. Zhang, K. Cheng, C. Wu, Y. Wang, H. Li, and X. Zhang, Implementing quantum search algorithm with metamaterials, *Advanced Materials* **30**, 1703986 (2018).

[46] C. Guo, M. Xiao, M. Minkov, Y. Shi, and S. Fan, Photonic crystal slab laplace operator for image differentiation, *Optica* **5**, 251 (2018).

[47] T. Zhu, Y. Lou, Y. Zhou, J. Zhang, J. Huang, Y. Li, H. Luo, S. Wen, S. Zhu, Q. Gong, *et al.*, Generalized spatial differentiation from the spin hall effect of light and its application in image processing of edge detection, *Physical Review Applied* **11**, 034043 (2019).

[48] F. Zangeneh-Nejad, D. L. Sounas, A. Alù, and R. Fleur, Analogue computing with metamaterials, *Nature Reviews Materials* **6**, 207 (2020).

[49] T. Zhu, J. Huang, and Z. Ruan, Optical phase mining by adjustable spatial differentiator, *Advanced Photonics* **2**, 016001 (2020).

[50] T. Zhu, C. Guo, J. Huang, H. Wang, M. Orenstein, Z. Ruan, and S. Fan, Topological optical differentiator, *Nature Communications* **12**, 680 (2021).

[51] D. Mattis, Solvable spin systems with random interactions, *Physics Letters A* **56**, 421 (1976).

[52] G. Genty, M. Surakka, J. Turunen, and A. T. Friberg, Second-order coherence of supercontinuum light, *Optics letters* **35**, 3057 (2010).

- [53] H. Nishimori, *Statistical physics of spin glasses and information processing: an introduction*, 111 (Clarendon Press, 2001).
- [54] N. Metropolis, A. W. Rosenbluth, M. N. Rosenbluth, A. H. Teller, and E. Teller, Equation of state calculations by fast computing machines, *The journal of chemical physics* **21**, 1087 (1953).
- [55] S. Jin, A. Sen, W. Guo, and A. W. Sandvik, Phase transitions in the frustrated ising model on the square lattice, *Physical Review B* **87**, 144406 (2013).
- [56] K. H. Fischer and J. A. Hertz, *Spin glasses*, 1 (Cambridge university press, 1993).

Supplementary Material: Wavelength-division multiplexing optical Ising simulator enabling fully programmable spin couplings and external magnetic fields

Li Luo, Zhiyi Mi, Junyi Huang, and Zhichao Ruan

*Interdisciplinary Center of Quantum Information,
State Key Laboratory of Modern Optical Instrumentation,
and Zhejiang Province Key Laboratory of Quantum Technology and Device,
Department of Physics, Zhejiang University, Hangzhou 310027, China*

I. DECOMPOSITION OF GENERAL ISING HAMILTONIAN INTO MULTIPLE MATTIS-TYPE MODELS

We first consider the Hamiltonian of Ising model without external magnetic field as $H = -\sum_{i \neq j}^N J_{ij} \sigma_i \sigma_j$, and N is the number of spins. To facilitate decomposition of the interaction matrix \mathbf{J} , we introduce auxiliary positive diagonal elements J_{ii} , and propose a Cholesky-like algorithm (Algorithm 1). This algorithm expresses \mathbf{J} as

$$[J_{ij}] = \xi^1 \times (\xi^1)^T + \xi^2 \times (\xi^2)^T + \xi^3 \times (\xi^3)^T + \cdots + \xi^N \times (\xi^N)^T \quad (S1)$$

where $\xi^1 = \begin{pmatrix} \xi_1^1 \\ \xi_2^1 \\ \xi_3^1 \\ \vdots \\ \xi_N^1 \end{pmatrix}$, $\xi^2 = \begin{pmatrix} 0 \\ \xi_2^2 \\ \xi_3^2 \\ \vdots \\ \xi_N^2 \end{pmatrix}$, $\xi^3 = \begin{pmatrix} 0 \\ 0 \\ \xi_3^3 \\ \vdots \\ \xi_N^3 \end{pmatrix}$, \dots , $\xi^N = \begin{pmatrix} 0 \\ 0 \\ 0 \\ \vdots \\ \xi_N^N \end{pmatrix}$. We note that the auxiliary diagonal elements J_{ii}

correspond to the self-interaction of spins, and only shift the energy value, without affecting the spin configurations of the ground state.

Algorithm 1: Cholesky-like decomposition

Input: Number of spins N , Interaction matrix $\mathbf{J} = \{J_{ij}\}$.

Output: Lower triangular matrix ξ , which satisfies $J_{jk} = \sum_{i=1}^N \xi_k^i \xi_k^i$ when $j \neq k$.

$$\text{Define } \xi = \begin{pmatrix} \xi_1^1 & \xi_1^2 & \cdots & \xi_1^N \\ \xi_2^1 & \xi_2^2 & \cdots & \xi_2^N \\ \vdots & \vdots & \ddots & \vdots \\ \xi_N^1 & \xi_N^2 & \cdots & \xi_N^N \end{pmatrix}_{N \times N} = \begin{pmatrix} 0 & 0 & \cdots & 0 \\ 0 & 0 & \cdots & 0 \\ \vdots & \vdots & \ddots & \vdots \\ 0 & 0 & \cdots & 0 \end{pmatrix}_{N \times N}, \mathbf{J}^{\text{now}} = \mathbf{J};$$

for $i = 1$ to N **do**

$$\xi_i^i = \sqrt{J_{ii}^{\text{now}}};$$

for $j = i + 1$ to N **do**

$$\xi_j^i = \frac{J_{ji}^{\text{now}}}{\xi_i^i};$$

end

$$\mathbf{J}^{\text{now}} = \mathbf{J}^{\text{now}} - \xi^i \times (\xi^i)^T;$$

end

We now consider the Ising model with an external magnetic field, given by the Hamiltonian $H = -\sum_{i \neq j}^N J_{ij} \sigma_i \sigma_j - \sum_i^N h_i \sigma_i$. To develop a Cholesky-like algorithm for this model, we add auxiliary elements θ^k to each vector $\kappa^1 =$

$$\begin{pmatrix} \xi_1^1 \\ \xi_2^1 \\ \xi_3^1 \\ \vdots \\ \xi_N^1 \\ \theta^1 \end{pmatrix}, \kappa^2 = \begin{pmatrix} 0 \\ \xi_2^2 \\ \xi_3^2 \\ \vdots \\ \xi_N^2 \\ \theta^2 \end{pmatrix}, \kappa^3 = \begin{pmatrix} 0 \\ 0 \\ \xi_3^3 \\ \vdots \\ \xi_N^3 \\ \theta^3 \end{pmatrix}, \dots, \kappa^N = \begin{pmatrix} 0 \\ 0 \\ 0 \\ \vdots \\ \xi_N^N \\ \theta^N \end{pmatrix}.$$

The values of θ^k are derived using Algorithm 2.

We further normalize each vector κ^k by dividing it by \sqrt{J} , where $J = \max\{|\kappa_j^k|^2\}$, so that $-1 \leq \kappa_j^k \leq 1$. Next, we introduce an auxiliary spin $\sigma_{N+1} = 1$ and rewrite the Hamiltonian as:

$$H = -J \sum_k^N \sum_{ij}^{N+1} \kappa_i^k \kappa_j^k \sigma_i \sigma_j + H_0 \quad (\text{S2})$$

where $H_0 = J \left(\sum_k^N (\xi_k^k)^2 + \sum_k^N (\theta^k)^2 \right)$.

Algorithm 2: Magnetic field encoding method

Input: Magnetic field parameter $\mathbf{h} = \{h_1, h_2, \dots, h_N\}$, lower triangular matrix $\boldsymbol{\xi}$.

Output: Lower triangular matrix $\boldsymbol{\kappa}$, which satisfies $J_{jk} = \sum_{i=1}^N \kappa_j^i \kappa_k^i$ when $j \neq k$, and $\sum_{i=1}^N \kappa_j^i \kappa_{N+1}^i = \frac{h_j}{2}$.

Define $\boldsymbol{\theta} = (\theta^1 \ \theta^2 \ \dots \ \theta^N)$;

for $i = 1$ **to** N **do**

$$\theta^i = \frac{\frac{h_i}{2} - \sum_{j=1}^{i-1} \theta^j \xi_i^j}{\xi_i^i};$$

end

II. GAUGE TRANSFORMATION AND OPTICAL COMPUTATION OF GENERAL ISING HAMILTONIAN

We first assume that the amplitude of the illumination light on SLM for each wavelength is uniform and equal to A_0 . For the k -th Mattis-type model, with the gauge transformation proposed in the main text, we encode each spin by $N_y \times N_x$ pixels as Fig. S1 and the phase modulation on SLM φ_j^k as defined in Eq.(2) in the main text. Therefore, the electric fields after the SLM modulation are given by

$$E_k(x, y) = iA_0(F_+ \cdot M_1 + F_- \cdot M_2) \quad (\text{S3})$$

where F_+ and F_- are written as

$$F_{\pm} = \sum_{j=k}^{N+1} e^{\pm i \alpha_j^k} \sigma_j \text{Rect}_{N_y W}(y - y_j) \cdot \text{Rect}_{N_x W}(x)$$

Here (x, y) denotes the spatial coordinate on the SLM plane, and $y_j = jN_y W$ represents the position of the j -th spin in y direction on SLM. The rectangular function is defined as

$$\text{Rect}_{N_y W}(y) = \text{Rect}\left(\frac{y}{N_y W}\right) = \begin{cases} 1, & |y| \leq N_y W/2 \\ 0, & |y| > N_y W/2 \end{cases} \quad (\text{S4})$$

where W represents the pixel width of the SLM. M_1 and M_2 are two checkerboard functions, as shown in Fig. S1, such that $M_1 + M_2 = 1$, and are defined as

$$\begin{aligned} M_1 &= \sum_{m,n=-\infty}^{\infty} [\delta(x - 2mW, y - 2nW) + \delta(x - (2m+1)W, y - (2n+1)W)] \otimes \text{Rect}_W(x, y) \\ M_2 &= \sum_{m,n=-\infty}^{\infty} [\delta(x - 2mW, y - (2n+1)W) + \delta(x - (2m+1)W, y - 2nW)] \otimes \text{Rect}_W(x, y) \end{aligned}$$

where \otimes denotes the convolution operation.

After passing through the Fourier lens, the optical fields at the CCD for each wavelength are evaluated using a two-dimensional Fourier transform. The resulting electric fields in the spatial spectra are given by:

$$\tilde{E}_k(k_x, k_y) = \frac{iA_0}{4} (G_+ \otimes P_1 + G_- \otimes P_2)$$

where

$$G_{\pm} = \sum_{j=k}^{N+1} e^{\pm i \alpha_j^k} \sigma_j \cdot \text{sinc}_{N_y W}(k_y) e^{ik_y y_j} \cdot (N_y W) \cdot \text{sinc}_{N_x W}(k_x) \cdot (N_x W)$$

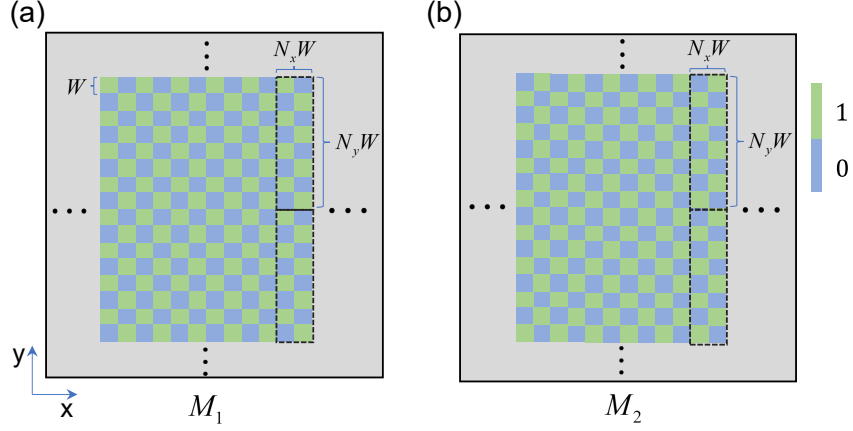


FIG. S1. (a) and (b) are the checkerboard functions M_1 and M_2 . Here each spin is encoded by $N_y \times N_x$ pixels as shown in the black dashed box. For the k -th Mattis-type model, the center of the j -th spin is located at $(kN_x W, jN_y W)$, where W represents the pixel width of the SLM.

$$P_1 = \sum_{m,n=-\infty}^{\infty} \left(1 + (-1)^{m+n}\right) \delta\left(k_x - m\frac{\pi}{W}, k_y - n\frac{\pi}{W}\right) \cdot \text{sinc}_W(k_x, k_y)$$

$$P_2 = \sum_{m,n=-\infty}^{\infty} ((-1)^m + (-1)^n) \delta\left(k_x - m\frac{\pi}{W}, k_y - n\frac{\pi}{W}\right) \cdot \text{sinc}_W(k_x, k_y)$$

$$\text{sinc}_W(k_x, k_y) = \text{sinc}\left(\frac{k_x W}{2\pi}\right) \cdot \text{sinc}\left(\frac{k_y W}{2\pi}\right)$$

$$\text{sinc}_{N_x W}(k_x) = \text{sinc}\left(\frac{k_x N_x W}{2\pi}\right)$$

$$\text{sinc}_{N_y W}(k_y) = \text{sinc}\left(\frac{k_y N_y W}{2\pi}\right)$$

$$\text{sinc}(k) = \frac{\sin(k\pi)}{k\pi}$$

Here, the convolution terms indicate that due to the checkerboard modulation, the beams are diffracted at multiple orders around $(m\frac{\pi}{W}, n\frac{\pi}{W})$ in the angular spectral space, where m and n are two integers. Assuming negligible field overlap between different orders, the zeroth order diffraction field for $m = 0$ and $n = 0$ can be expressed as

$$\tilde{E}_k(k_x, k_y) \doteq i A_0 C \sum_{j=k}^{N+1} \kappa_j^k \sigma_j e^{ik_y y_j} \text{sinc}_W(k_x, k_y) \text{sinc}_{N_x W}(k_x) \text{sinc}_{N_y W}(k_y) \quad (\text{S5})$$

where $C = N_x W \cdot N_y W$.

For the angle spectrum (k_x, k_y) , the spatial coordinate (u_x, u_y) on the detection plane are $u_x = k_x \frac{f\lambda}{2\pi}$, $u_y = k_y \frac{f\lambda}{2\pi}$. Thus, the intensity contributed by the k -th wavelength light is given by

$$\begin{aligned} I_k(u_x, u_y) &= \tilde{E}_k^* \cdot \tilde{E}_k \\ &= A_0^2 C^2 \sum_{i,j=k}^{N+1} \kappa_i^k \kappa_j^k \sigma_i \sigma_j e^{i \frac{2\pi}{f\lambda} u_y (y_j - y_i)} \text{sinc}^2\left(\frac{u_x W}{f\lambda}\right) \text{sinc}^2\left(\frac{u_y W}{f\lambda}\right) \text{sinc}^2\left(\frac{u_x W N_x}{f\lambda}\right) \text{sinc}^2\left(\frac{u_y W N_y}{f\lambda}\right) \end{aligned}$$

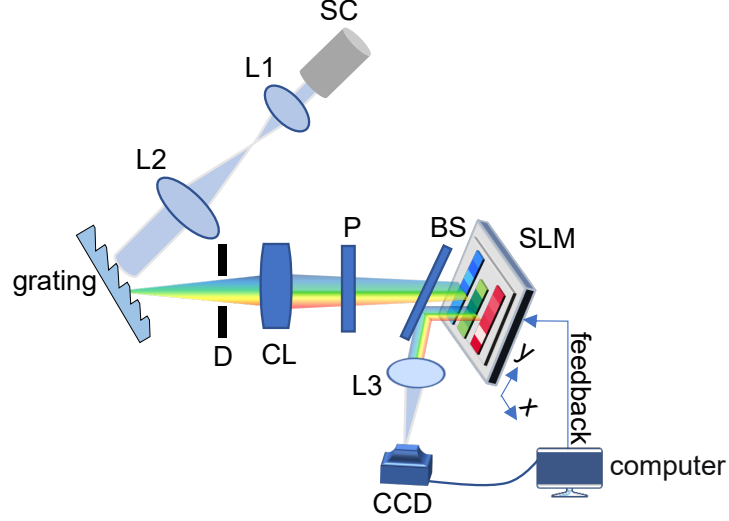


FIG. S2. Experimental setup of the wavelength-division multiplexing optical Ising simulator. SC: super-continuum laser; L1, L2 and L3: Fourier lens; D: diaphragm; CL: cylindrical lens; P: polarizer; BS: beam splitter; SLM: spatial light modulator; CCD: charge-coupled device.

In particular, the intensity at $u_x = 0$ and $u_y = 0$ is

$$I_k(0,0) = A_0^2 C^2 \sum_{i,j=k}^{N+1} \kappa_i^k \kappa_j^k \sigma_i \sigma_j \quad (\text{S6})$$

Due to the incoherent nature between different wavelengths, the total intensity detected at the zeroth order is

$$\begin{aligned} I &= \sum_k^N I_k(0,0) \\ &= A_0^2 C^2 \sum_k^N \sum_{i,j=k}^{N+1} \kappa_i^k \kappa_j^k \sigma_i \sigma_j \end{aligned} \quad (\text{S7})$$

For a special case of $\{\kappa_j^k = 1\}$ and $\{\sigma_j = 1\}$ for all spins, the phase modulations are given by $\{\varphi_j^k = \frac{\pi}{2}\}$ (see Eq. (2) in the main text). That is, when the phase modulation is set to $\frac{\pi}{2}$ for all pixels, the intensity on CCD is $I_0 = A_0^2 C^2 N(N+1)^2$. Therefore by measuring the intensities and normalizing the intensity to I_0 , the Ising Hamiltonian for the general spin interaction is optically computed as

$$\tilde{I} = N(N+1)^2 \frac{I}{I_0} = \sum_k^N \sum_{i,j=k}^{N+1} \kappa_i^k \kappa_j^k \sigma_i \sigma_j \quad (\text{S8})$$

We note that when the amplitude for different wavelengths is not uniform, supposing that the amplitude for the k -th wavelength is A_k , the phase encoding in Eq. (2) can be modified as $\alpha_j^k = \arccos \frac{\kappa_j^k}{A_k}$. Here A_{\min} is the minimum amplitude among all wavelengths. Under such circumstances, the above derivation is still available, but the normalized intensity I_0 changes to $I_0 = A_{\min}^2 C^2 N(N+1)^2$.

III. EXPERIMENTAL SETUP AND MEASUREMENT OF INTENSITY

Figure S2 illustrates the experimental setup of the wavelength-division multiplexing optical Ising simulator. Here a super-continuum laser (Anyang SC-5) is used to generate a collimated Gaussian beam. The waist radius of the light beam is enlarged tenfold by the lens L_1 (focal length is 50mm) and L_2 (focal length is 500mm). The light

then illuminates a reflective diffraction grating (inscribed line density of 600/mm), and the cylindrical lens (CL, the focal length is 100mm) focuses the light with different wavelengths onto the SLM (Holoeye PLUTO-NIR-011). With this configuration, the light with different wavelengths is diffracted along the x direction of the SLM, while the y -directional pixels are coherently illuminated by the collimated incident light with the same wavelength. An adjustable diaphragm is designed to change the wavelength range incident on the SLM. For the $\pm J$ model and Sherrington-Kirkpatrick (SK) models (Figure 2 in the main text) 80 spins cover wavelengths from 588nm to 611nm, with each spin occupying $\Delta\lambda = 0.3\text{nm}$ in the x direction. For the J_1-J_2 model (Figs. 3-4 in the main text), we carry out experiments with 64 spins and set $\kappa_j^k = 0$ and $\sigma_j = 1$ for the other 16 spins. According to Eq. (S6), $\kappa_j^k = 0$ results in no contribution of σ_j to $I_k(0,0)$. Polarizer P is used to make the incident beam linearly polarized along the long display axis of the SLM.

Lens L_3 (200mm focal length) performs a Fourier transformation of the optical field from the SLM. A CCD (Ophir SP620) is placed at the back focus plane to detect optical field intensity. Due to the finite size of SLM pixel and the resolution of CCD, we integrate the intensity within a region around the center point instead of measuring the intensity at a single point. The effective squared detection area A is defined as $|u_x|, |u_y| < \frac{d}{2}$. We find that the results are convergent and stable when $d = 45\mu\text{m}$, which corresponds to a detection area covering 10×10 pixels.